Steering the optimization pathway in the control landscape using constraints

José P. Palao,[1] Daniel M. Reich,[2] and Christiane P. Koch[2]

[1]*Departamento de Física Fundamental II and IUdEA, Universidad de La Laguna, 38204 La Laguna, Spain*
[2]*Theoretische Physik, Universität Kassel, Heinrich-Plett-Strasse 40, 34132 Kassel, Germany*

We show how additional constraints, restricting the spectrum of the optimized pulse or confining the system dynamics, can be used to steer optimization in quantum control towards distinct solutions. Our examples are multiphoton excitation in atoms and vibrational population transfer in molecules. We show that a spectral constraint is most effective in enforcing nonresonant two-photon absorption pathways in atoms and avoiding unnecessarily broad spectra in Raman transitions in molecules. While a constraint restricting the system to stay in an allowed subspace is also capable of identifying nonresonant excitation pathways, it does not avoid spurious peaks in the pulse spectrum. Both constraints are compatible with monotonic convergence but imply different additional numerical costs.

I. INTRODUCTION

Quantum optimal control utilizes shaped external fields to reach a desired target in the best possible way [1]. It has been successfully applied in a variety of settings, from femtosecond laser spectroscopy to nuclear magnetic resonance or quantum information processing; see Ref. [2] and references therein for a recent overview. The enormous success of quantum control, both in optimal control theory [3] and adaptive feedback control experiments [4], has been rationalized in terms of the favorable properties of the control landscape [5]. This landscape visualizes the optimization target as a function of the control parameters. Optimization corresponds to a search for the maxima or minima in the landscape. Success of control is explained by broad peaks that can easily be climbed [6]. Suboptimal peaks, while not completely excluded [7], seem to play no significant role in actual control applications. The intuitive picture of the control landscape can not only elucidate search pathways but also help to find the mechanism underlying an optimized control field. It is thus not surprising that the theoretical concept has triggered a number of experimental investigations [8–10].

Any experiment is, however, subject to constraints such as finite pulse power, bandwidth, and time or frequency resolution. These constraints will necessarily make some of the optimal peaks in the landscape inaccessible and may lead to traps and saddle points [11]. In order to search for control solutions in optimal control theory that can be realized in a given experiment, the experimental constraints should be included as additional costs in the optimization functional. For example, the system dynamics can be restricted to a certain subspace in order to block undesired strong-field effects or avoid decoherence [12]. Formulating the additional costs is not always straightforward. In particular, imposing conditions simultaneously on the spectrum and the shape of an optimized pulse has proven to be challenging [13–17]. Although they exclude part of the ideal control landscape [11], additional constraints are not necessarily detrimental. They can also be used to actively steer the optimization pathway toward a particular solution out of several available ones. This is the subject of our current work.

We employ spectral constraints, imposing filters on the optimized spectrum [13], and state-dependent constraints,

restricting the system dynamics to a subspace [12], to optimize for nonresonant excitation in atoms and vibrational population transfer in molecules. Unless one employs a two-photon rotating wave approximation which excludes resonant one-photon pathways *a priori*, finding nonresonant transitions poses a notoriously difficult problem in optimal control theory since it contradicts the condition of minimal power consumption. This is particularly dissatisfying in view of the many experimental studies of nonresonant two-photon absorption for *ns* to $(n + 1)s$ transitions in alkali-metal atoms in the weak- [18–20], strong- [21–23] and intermediate-field regimes [24–27]. To date, only solutions using one-photon transitions are found, while the experimental result of *nonresonant* two-photon control [18–27] could not be reproduced. Here we employ optimal control theory using Krotov's method [28–30] and impose spectral and state-dependent constraints to enforce a nonresonant two-photon solution. We then extend our study to vibrational population transfer. For this example, optimal control calculations have also been hampered by an enormous spectral spread of the field, so much so that the resulting spectral widths by far exceed experimentally realistic values [14,31]. We show that for both examples, a spectral constraint successfully suppresses all undesired frequency components.

The paper is organized as follows: Section II presents a brief review of Krotov's method for quantum optimal control. Special emphasis is placed on how to include additional constraints in a way that preserves monotonic convergence. Multiphoton absorption in sodium atoms is studied in Sec. III for two different optimization targets—maximizing two-photon absorption and generating a third harmonic with near-infrared light. The problem of broad spectral widths in vibrational population transfer in molecules is studied in Sec. IV. Section V summarizes our findings.

II. CONSTRAINTS IN KROTOV'S METHOD

We briefly review optimization using Krotov's method following Refs. [12,13,28]. An optimization problem is defined in terms of the equation of motion,

$$\frac{d}{dt}|\psi(t)\rangle = -\frac{i}{\hbar}\hat{\mathsf{H}}[\epsilon(t)]|\psi(t)\rangle, \qquad (1)$$

and the optimization functional,

$$J[\{\psi_k\},\epsilon] = J_T[\{\psi_k(T)\}] + J_a[\epsilon] + J_b[\{\psi_k\}], \quad (2)$$

which consists of the target and additional constraints. Here J_T is the target functional, evaluated at final time T, and $\{\psi_k(t)\}$ are a set of state vectors which all fulfill Eq. (1). $\epsilon(t)$ represents the control variable, e.g., the electric field of a laser pulse. The additional constraints are assumed to depend either on the control or on the states,

$$J_a = \int_0^T g_a(\epsilon,t)dt, \quad (3)$$

$$J_b = \int_0^T g_b(\{\psi_k\},t)dt. \quad (4)$$

We first present the optimization equations for the most general form of $g_a(\epsilon,t)$ preserving monotonic convergence in Sec. II A, followed by a discussion of optimization under state-dependent constraints $g_b(\{\psi_k\},t)$ in Sec. II B.

A. Spectral constraints

We have recently shown that a monotonically converging optimization algorithm is obtained if the constraint depending on the control is formulated in terms of a positive semidefinite kernel [13],

$$g_a(\epsilon,t) = \frac{1}{2\pi}\int_0^T \Delta\epsilon(t)K(t-t')\Delta\epsilon(t')dt', \quad (5a)$$

$$\bar{K}(\omega) \geqslant 0 \ \forall \ \omega, \quad (5b)$$

where $\bar{K}(\omega)$ is the Fourier transform of $K(t-t')$. In this way, one can enforce constraints which depend both on time and frequency. Since the derivation of the update equation requires evaluation of $\frac{\partial g_a}{\partial\epsilon}$ as a function of time [28,29,32], the Fourier

transform of $\bar{K}(\omega)$ should have a closed form in addition to being positive semidefinite. An obvious choice is Gaussian kernels,

$$\bar{K}(\omega) = \lambda_a^0 - \sum_j \frac{\lambda_a^j}{2}\left[e^{-\frac{(\omega-\omega_j)^2}{2\sigma_j^2}} + e^{-\frac{(\omega+\omega_j)^2}{2\sigma_j^2}}\right], \quad (6a)$$

$$K(t-t') = 2\pi\lambda_a^0\delta(t-t')$$
$$- \sum_j \lambda_a^j\sqrt{2\pi\sigma_j^2}\cos[\omega_j(t-t')]e^{-\frac{\sigma_j^2(t-t')^2}{2}}, \quad (6b)$$

which come with the additional advantage of smoothness which is desirable in view of numerical stability. For (approximately) nonoverlapping Gaussians in frequency domain, monotonic convergence is obtained if

$$\lambda_a^j \leqslant 2\lambda_a^0 \ \forall \ j \neq 0. \quad (7)$$

Note that we assume real pulses in Eq. (6a), which is why the kernel is symmetric. An extension to complex pulses is straightforward by mapping it to a real pulse on a time grid of twice the size. The first term in Eq. (6b) reproduces the standard choice for g_a which minimizes the change in intensity [32] with constant shape function. For $\lambda_a^j > 0$ ($\lambda_a^j < 0$), the kernel (6b) implements a frequency pass (filter) for $\Delta\epsilon(t)$ around the frequencies ω_j. Due to the condition (7), the strength of frequency passes that still allows for monotonic convergence is restricted. This reduces their effectiveness in practice, and frequency passes should rather be enforced by expressing them as a sum over many frequency filters. An amplitude constraint with nonconstant shape function $S(t)$ can be reintroduced additively in time domain for $\lambda_a^j < 0$, setting $\lambda_a^0 = 0$. The update equation for the control at iteration $i+1$ for Gaussian band filters and an additional amplitude constraint imposed by a shape function $\lambda_0/S(t)$ is obtained as

$$\epsilon^{(i+1)}(t) = \epsilon^{(i)}(t) + \sum_j \frac{\lambda_a^j S(t)}{2\pi\lambda_0}\sqrt{2\pi\sigma_j^2}\int_0^T \cos[\omega_j(t-t')]e^{-\frac{\sigma_j^2(t-t')^2}{2}}[\epsilon^{(i+1)}(t') - \epsilon^{(i)}(t')]dt'$$

$$+ \frac{S(t)}{\lambda_0}\text{Im}\left\{\sum_k \langle\chi_k^{(i)}(t)|\frac{\partial\hat{H}}{\partial\epsilon}|\psi_k^{(i+1)}(t)\rangle + \frac{1}{2}\sigma(t)\sum_k \langle\Delta\psi_k(t)|\frac{\partial\hat{H}}{\partial\epsilon}|\psi_k^{(i+1)}(t)\rangle\right\}, \quad (8)$$

where $|\Delta\psi_k(t)\rangle$ is the change in state from iteration i to $i+1$, i.e., $|\Delta\psi_k(t)\rangle = |\psi_k^{(i+1)}(t)\rangle - |\psi_k^{(i)}(t)\rangle$.

The adjoint states $\{\chi_k(t)\}$ are subject to the same equations of motion, given by Eq. (1), as the $\{\psi_k(t)\}$, but their "initial" condition is given at the final time T, i.e., they are propagated backward in time. The specific form of the initial condition is determined by the final-time target,

$$\left|\chi_k^{(i)}(T)\right\rangle = -\nabla_{\langle\psi_k|}J_T\big|_{\{\psi_k^{(i)}(T)\}}, \quad (9)$$

which is evaluated using the forward-propagated states $\{|\psi_k^{(i)}(T)\rangle\}$.

In the examples presented below, we assume the interaction with the control to be linear,

$$\hat{H}[\epsilon] = \hat{H}_0 + \hat{\boldsymbol{\mu}}\epsilon(t), \quad (10)$$

and the target functional to be convex in the states. The latter allows for the choice $\sigma(t) \equiv 0$, and Eq. (8) reduces to

$$\epsilon^{(i+1)}(t) = \epsilon^{(i)}(t) + \frac{S(t)}{\lambda_0}\text{Im}\left\{\sum_k \langle\chi_k^{(i)}(t)|\hat{\boldsymbol{\mu}}|\psi_k^{(i+1)}(t)\rangle\right\}$$

$$+ \sum_j \frac{\lambda_a^j S(t)}{2\pi\lambda_0}\sqrt{2\pi\sigma_j^2}\int_0^T \cos[\omega_j(t-t')]e^{-\frac{\sigma_j^2(t-t')^2}{2}}[\epsilon^{(j+1)}(t') - \epsilon^{(j)}(t')]dt', \quad (11)$$

with the third term due to the spectral constraint. In order to solve Eq. (11) which is implicit in $\epsilon^{(i+1)}(t)$, we rewrite it as a Fredholm integral equation of the second kind in $\Delta\epsilon(t) = \epsilon^{(i+1)}(t) - \epsilon^{(i)}(t)$,

$$\Delta\epsilon(t) = I(t) + \gamma \int_0^T \mathcal{K}(t,t')\Delta\epsilon(t')dt'. \qquad (12)$$

The inhomogeneity $I(t)$ depends on the unknown states $\{\psi_k^{(i+1)}(t)\}$; cf. Eq. (11). We approximate them by calculating $\Delta\epsilon(t)$ without frequency constraints and solve the Fredholm equation, mapped from the interval $[0,T]$ to $[0,1]$, using the method of degenerate kernels with triangularly shaped basis functions [33,34]. This corresponds to writing $\mathcal{K}_N(t,t') = \sum_{j,k=0}^N \alpha_j(t)\beta_k(t')$ for an Nth-order approximation with

$$\alpha_j(t) = \begin{cases} 1 - N\left|t - \frac{j}{N}\right|, & \frac{j-1}{N} \leqslant t \leqslant \frac{j+1}{N} \\ 0 & \text{else,} \end{cases} \qquad (13)$$

with $\beta_j(t) = \alpha_j(t)$ and solving a system of linear equations,

$$[\mathbb{1}_{N+1} - \gamma\mathsf{C}]\vec{X} = \gamma\vec{b}, \qquad (14)$$

with matrix elements

$$C_{jk} = \sum_{i=0}^n K(t_j,t_i)\int_0^1 \alpha_i(t)\alpha_k(t)dt \equiv \sum_{i=0}^n K(t_j,t_i)A_{ik},$$

where

$$A_{ik} = \begin{cases} \frac{1}{3n} & \text{for} \quad i = k = 0 \text{ or } i = k = n \\ \frac{2}{3n} & \text{for} \quad i = k, 1 \leqslant i \leqslant n \\ \frac{1}{6n} & \text{for} \quad i = k+1 \text{ or } i = k-1 \\ 0 & \text{else,} \end{cases}$$

and

$$b_k = \int_0^1 I(t)\left[\sum_{i=0}^n K(t_k,t_i)\alpha_i(t)\right]dt.$$

The solution to Eq. (12) is then given by

$$\Delta\epsilon(t) = I(t) + \sum_{j=0}^N X_j\alpha_j(t), \qquad (15)$$

where X_j is the solution of Eq. (14).

To summarize, optimization in the presence of spectral constraints proceeds in two steps: It requires forward (backward) propagation of the states $|\psi_k(t)\rangle$ (adjoint states $|\chi_k(t)\rangle$) according to Eq. (1) and evaluation of the update, given by Eq. (11), without the spectral constraint, i.e., $\lambda_a^j = 0$ for all j. This yields the input for $I(t)$ in Eq. (12) which is solved in the second step.

B. State-dependent constraints

State-dependent constraints can be employed to optimize a time-dependent expectation value or enforce the system to stay within a subspace of the total Hilbert space [12]. It takes the form

$$g_b(\{\psi_k(t)\},t) = \lambda_b \sum_{k=1}^N \langle\psi_k(t)|\hat{D}(t)|\psi_k(t)\rangle, \qquad (16)$$

where the dependence on the states is quadratic. We will employ, in the examples below, $\hat{D}(t) = \hat{P}_{\text{allow}}$. For this specific choice, $\sigma(t)$ in Eq. (8) can be set to zero, and the update for the control is again given by Eq. (11), possibly with $\lambda_a^j = 0$ for all j. Any other choice of $\hat{D}(t)$ requires nonzero $\sigma(t)$ and use of Eq. (8) as discussed in Ref. [28].

A state-dependent constraint does not only affect the update equation for the control via $\sigma(t)$, but also the equation of motion for the adjoint states which follows from the first-order extremum condition on the optimization functional [12]. When evaluating the derivatives, an additional dependence of the optimization functional on the states due to g_b yields an additional term in the equation of motion. The corresponding inhomogeneous Schrödinger equation reads

$$\frac{d}{dt}|\chi(t)\rangle = -\frac{i}{\hbar}\hat{H}[\epsilon(t)]|\chi(t)\rangle + \lambda_b\hat{P}_{\text{allow}}|\psi(t)\rangle. \qquad (17)$$

It is evaluated for the "old" control, $\epsilon^{(i)}(t)$, and the "old" state, $|\psi^{(i)}(t)\rangle$, and can be solved by a modified Chebychev propagator [35].

To summarize, optimization in the presence of state-dependent constraints requires forward propagation of the states $|\psi_k(t)\rangle$ according to Eq. (1), solution of an inhomogeneous Schrödinger equation, given by Eq. (17), for the backward propagation of the adjoint states $|\chi_k(t)\rangle$, and evaluation of the update, given by Eq. (11).

III. CONTROL OF NONRESONANT TWO-PHOTON ABSORPTION

We compare Krotov's method using a spectral constraint and using a state-dependent constraint to maximize the nonresonant two-photon absorption in sodium atoms. Our model,

$$\hat{H}[\epsilon] = \sum_j \omega_j|j\rangle\langle j| + \epsilon(t)\sum_{i\neq j}\mu_{ij}|j\rangle\langle i|, \qquad (18)$$

is comprised of the levels $|j\rangle = |3s\rangle$, $|4s\rangle$ and $|np\rangle$ ($n = 3,\ldots,8$) and all $|ns\rangle \rightarrow |n'p\rangle$ dipole-allowed transitions. The energies and dipole moments are taken from Ref. [36]. For the spectral constraint, forward and backward propagation involve solution of the standard time-dependent Schrödinger equation, given by Eq. (1), which is carried out by a Chebychev propagator [37]. In contrast, for the state-dependent constraint, an inhomogeneous Schrödinger equation [cf. Eq. (17)] governs the backward propagation. It can be solved with a modified Chebychev propagator [35] which is most efficient when high accuracy is desired. Here, we simply utilize a zeroth-order approximation as discussed in Ref. [12]: We calculate $\exp[i\hat{H}\Delta t]|\chi(t_i)\rangle$ by diagonalization of the Hamiltonian with the time dependence evaluated at $t_i + \Delta t$ and assumed constant over Δt. The inhomogeneous term in Eq. (17) is approximated by $\lambda_b/2[\hat{P}_{\text{allow}}|\psi(t_i)\rangle + \hat{P}_{\text{allow}}|\psi(t_{i+1})\rangle]$. We use 4096 time grid points, ensuring a sufficiently small Δt for the approximation to be valid. The guess pulse is chosen to be Gaussian centered around the two-photon transition frequency, $\omega_{3s,4s}/2$. The shape function, $S(t)$ in Eq. (8), takes the form $S(t) = \sin^2(\pi t/T)$.

We consider two different targets to maximize population in $|4s\rangle$ and in $(|3s\rangle + |7p\rangle)/\sqrt{2}$. The $|7p\rangle$ state is reached
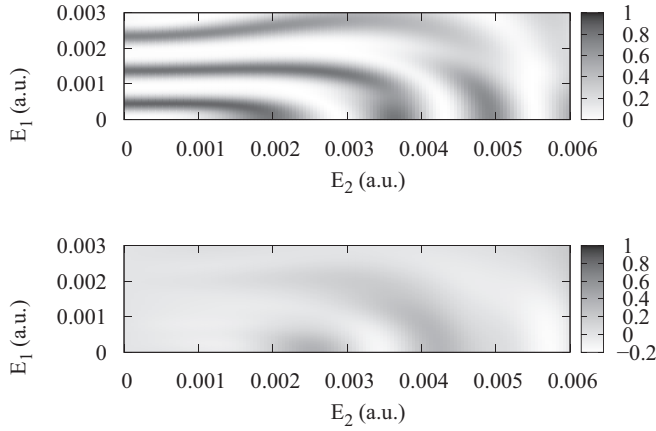
FIG. 1. Transition probability landscape for nonresonant two-photon absorption ($\langle 4s|4s\rangle$, top) and harmonic generation ($2\mathrm{Re}\left[\langle 7p|3s\rangle\right]$, bottom) for transform-limited 50 fs Gaussian pulses, parametrized by Eq. (19).
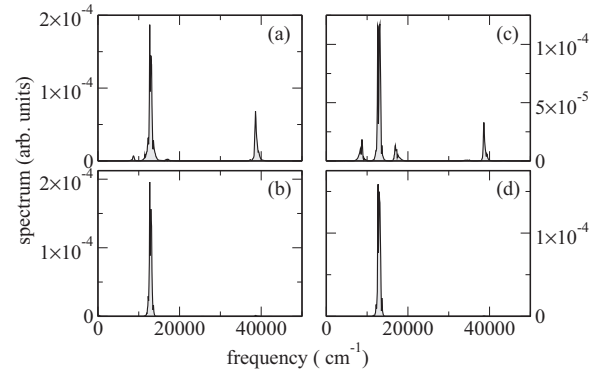

FIG. 2. Control of nonresonant two-photon absorption: Optimized spectra with (b),(d) and without (a),(c) bandwidth constraint ($\lambda_0 = 400$ left, $\lambda_0 = 1000$ right). The bandwidth constraint consists of filters at $\omega_{3s,3p}$, $\omega_{3p,4s}$, $3\omega_L$, and $5\omega_L$ (where $\omega_L = \omega_{3s,4s}/2$) with $\sigma_i = 0.004$ a.u. and $\lambda_a^i = 10^6 \; \forall i$.

from the ground $|3s\rangle$ state by a (2+1) transition via the $|4s\rangle$ state using near-infrared photons [23,38,39]. The target $(|3s\rangle + |7p\rangle)/\sqrt{2}$ yields a maximum transition dipole between $|3s\rangle$ and $|7p\rangle$ and thus corresponds to maximizing harmonic generation of ultraviolet light [40].

The constraints are necessary since two obvious control strategies are available—resonant two-color one-photon transitions with frequencies $\omega_{3s,3p}$ and $\omega_{3p,4s}$ or off-resonant two-photon transitions with frequencies close to $\omega_{3s,4s}/2$. This is illustrated by Fig. 1 which displays the two figures of merit, i.e., population of $|4s\rangle$ and maximum coherence on the $|3s\rangle \rightarrow |7p\rangle$ transition at the end of the pulse, as a function of one-photon and two-photon amplitudes. The visualization of the control landscape is based on parametrizing the field by

$$E(t) = e^{-\frac{(t-T)^2}{2\tau^2}} \{E_1[\cos(\omega_{3s,3p}t) + \cos(\omega_{3p,4s}t)]$$
$$+ E_2 \cos(\omega_{3s,4s}t/2)\}. \quad (19)$$

The two different solutions, i.e., resonant one-photon transitions and nonresonant two-photon transitions, are clearly visible in the upper panel of Fig. 1. A possible solution to achieving maximum population in $|4s\rangle$ is a two-photon π pulse [41]. For one-photon transitions, this requires equal Rabi frequencies on both transitions [41]. Since the transition dipole moments for the $|3s\rangle \rightarrow |3p\rangle$ and the $|3p\rangle \rightarrow |4s\rangle$ transitions are fairly similar, this condition can almost be fulfilled even by identical E_1 on both transitions, as assumed in Eq. (19). Correspondingly, a series of dark shaded regions is found in Fig. 1 for $E_2 = 0$, for a two-photon π pulse, 3π pulse and 5π pulse. The population of $|4s\rangle$ becomes smaller as E_1 is increased. This is due to the dynamic Stark shift getting larger and shifting the transition off-resonance. Analogously to the series of dark shaded regions as a function of E_1 for $E_2 = 0$, a similar series is found as a function of E_2 for $E_1 = 0$. The amplitude for a nonresonant two-photon π pulse with a duration of 50 fs corresponds to $E_2 = 0.00201$ a.u. Since our parametrization allows only for transform-limited pulses, population transfer is not complete at this value of E_2. This is again due to the large dynamic Stark shift. It can be compensated by chirping the pulse [21] but, for the sake of

a simple pulse parametrization that allows for visualizing the control landscape in terms of two parameters, we only analyze transform-limited pulses. Another reason for the population in $|4s\rangle$ to be smaller than one is population leakage to $|7p\rangle$ since the transition energy $\omega_{4s,7p}$ is very close to $\omega_{3s,4s}/2$. When both E_1 and E_2 are nonzero, the purely one-photon and purely two-photon solutions are smoothly connected by pulses which contain both spectral components. The lower panel of Fig. 1 illustrates that the solution to maximizing coherence on the $|3s\rangle \rightarrow |7p\rangle$ transition is less obvious.

We discuss now how the spectral constraints can be used to steer the optimization pathway in the control landscape shown in the upper panel of Fig. 1. Our guess pulse is of the form (19) with $E_1 = 0$, $E_2 = 0.0005$ a.u., and a pulse duration of 50 fs. For this guess pulse, there are two possible pathways: increasing the intensity to obtain a two-photon solution, i.e., moving along the E_2 axis, or adding new frequencies to the pulse to obtain the resonant $|3s\rangle \rightarrow |3p\rangle$ and $|3p\rangle \rightarrow |4s\rangle$ transitions, i.e., moving along the E_1 axis. Once the guess pulse is fixed, the only free parameter in the standard Krotov method is λ_0, which determines the step size for changes in the control; cf. Eq. (11). For this simple example, it turns out that the choice of λ_0 is sufficient to steer the optimization pathway in one of the two possible directions (cf. Fig. 2): A small value of λ_0 allows for finding the two-photon solution, i.e., no peaks at the one-photon frequencies, $\omega_{3s,3p} = 16\,956$ cm^{-1} and $\omega_{3p,4s} = 8766$ cm^{-1}, are observed in Fig. 2(a), whereas for a large value of λ_0, these peaks are present [cf. Fig. 2(c)]. Figure 3 displaying the population dynamics under the optimized fields of Fig. 2 confirms this interpretation: The $|3p\rangle$ state is populated significantly at intermediate times in Fig. 3(c). A small value of λ_0 is, however, not very useful in general since it often leads to "exotic" solutions with spurious peaks at harmonics of the laser frequency, such as the peaks at $3\omega_L$ and $5\omega_L$ in Fig. 2 (the latter being outside of the figure's scale). In our simple example, these peaks can simply be removed from the spectrum without compromising the figure of merit or affecting the population dynamics. However, as we show below, this is not always the case. The solution is then an increase in λ_0, but this implies that any capability of steering
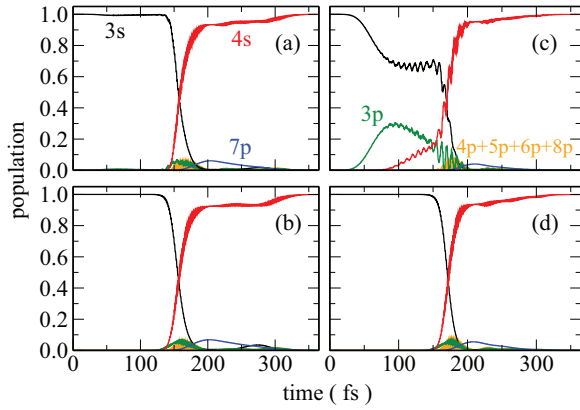
FIG. 3. (Color online) Control of nonresonant two-photon absorption: Population dynamics under the optimized fields (b),(d) with and (a),(c) without bandwidth constraint ($\lambda_0 = 400$ left, $\lambda_0 = 1000$ right) as shown in Fig. 2.

the optimization pathway in the algorithm without additional constraints is lost.

The situation changes when the spectral constraint is included in the optimization functional; cf. Figs. 2(b) and 2(d). No matter what the value of λ_0 is, a pure two-photon solution is found. Additionally, the spurious peaks at the higher harmonics can be suppressed by adding a filter at the corresponding frequencies. The nonresonant character of the excitation is confirmed by Figs. 3(b) and 3(d), where almost no population in $|3p\rangle$ is observed. Moreover, the population leakage to higher $|p\rangle$ states is slightly smaller in Figs. 3(b) and 3(d) than in Figs. 3(a) and 3(b).

The enhanced functionality of Krotov's method including spectral constraints comes at a price. This is illustrated by Fig. 4, which shows how the final-time target J_T functional approaches its optimum, $J_T = 1$. Independently of the value of λ_0, more iterations are required when the spectral constraint, which makes the control problem harder, is included. However, the increase in the number of iterations is very moderate. The actual additional computational cost due to the spectral constraint depends on the complexity of the quantum system. In the current example, the forward and backward propagations are numerically very inexpensive. The solution of the Fredholm equation (12) then represents a significant computational overhead [13]. However, for complex quantum systems, propagation of the states and adjoint states requires by far most of the numerical effort, and the additional cost of solving the Fredholm equation becomes negligible. Figure 4
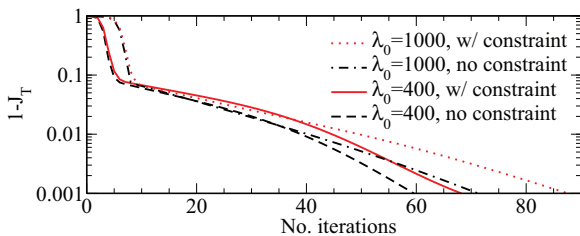

FIG. 4. (Color online) Convergence toward the optimum with and without spectral constraint for two-photon absorption and two different optimization step sizes.
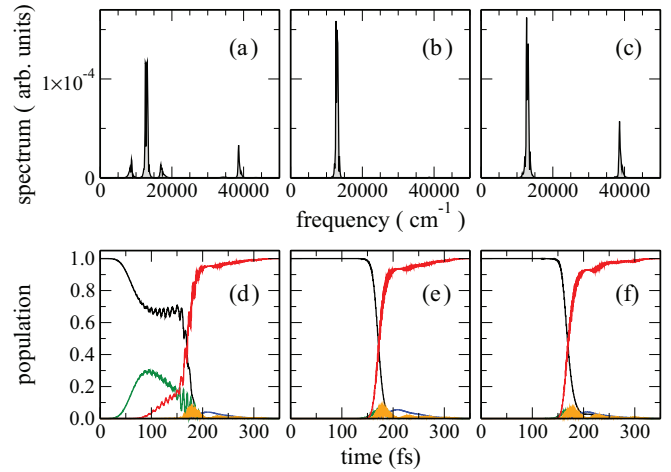

FIG. 5. (Color online) Control of two-photon absorption: (a)–(c) Spectra and (d)–(f) population dynamics for optimization with (b),(e) spectral, (c),(f) state-dependent, and (a),(d) no constraint for a 50 fs guess pulse with $E_2 = 0.0005$ a.u., $\lambda_0 = 1000$, and $\lambda_b T = -1$. The same filters and λ_a^i for the spectral constraint as in Fig. 2 and the same color coding for the population dynamics as in Fig. 3 are used.

also shows a faster convergence for a smaller value of λ_0. This is not surprising since a smaller value of λ_0 implies a larger change in the control; cf. Eq. (11).

The control strategy using resonant two-color one-photon transitions populates the $|3p\rangle$ state; cf. Fig. 3(c). Alternatively to employing a spectral constraint, it should therefore be possible to enforce a nonresonant two-photon solution with a state-dependent constraint that suppresses the population of $|3p\rangle$ at any time. To this end, we define the allowed subspace to be spanned by $|3s\rangle$ and $|4s\rangle$ and maximize population in this subspace for all times using a state-dependent constraint. Figure 5 compares optimization of two-photon absorption without any additional constraint [Figs. 5(a) and 5(d)] to that with the spectral constraint used before [Figs. 5(b) and 5(e)] and the state-dependent constraint just defined [Figs. 5(c) and 5(f)]. The peak amplitude of the initial Gaussian guess pulse corresponds to a two-photon $\pi/4$ pulse. Both optimizations with an additional constraint avoid population of the $|3p\rangle$ state completely; cf. the green lines in the lower part of Fig. 5. Correspondingly, the one-photon peaks at $\omega_{3s,3p} = 16\,956$ cm^{-1} and $\omega_{3p,4s} = 8766$ cm^{-1} are missing in the spectrum obtained with the state-dependent constraint in Fig. 5(c). However, only the spectrum obtained with the spectral constraint in Fig. 5(b) corresponds to a pure two-photon solution. This observation emphasizes that one should use a mathematical formulation of the constraint that best captures the physical goal, in our case the nonresonant two-photon solution.

Maximizing the $|3s\rangle \rightarrow |7p\rangle$ transition dipole represents a somewhat harder optimization problem than maximizing two-photon absorption, and transform-limited pulses are not sufficient to approach the optimum; cf. the lower panel of Fig. 1. The difficulty of the optimization problem is reflected in the fact that optimization without any additional constraint always yields spectra that contain the one-photon peaks at $\omega_{3s,3p} = 16\,956$ cm^{-1} and $\omega_{3p,4s} = 8766$ cm^{-1}; cf. the upper panel of Fig. 6. This is true even for very large values of λ_0, up
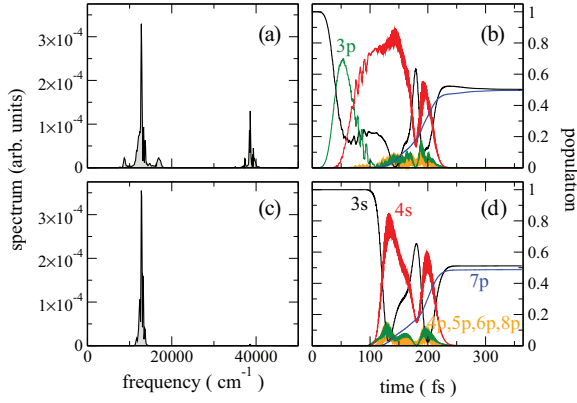
FIG. 6. (Color online) Control of harmonic generation: Spectrum and population dynamics for optimization (c),(d) with and (a),(b) without spectral constraint for $\lambda_0 = 400$ and a 50 fs guess pulse with $E_2 = 0.00201$ a.u. The same filters and λ_a^i as in Fig. 2 are used.

to 100 000, that imply a very cautious search in small steps. The one-photon character of the transition is confirmed by the large population of $|3p\rangle$, up to 70% at about $t = 50$ fs, shown in Fig. 6(b). In addition to the two-photon and one-photon peaks, a peak at $3\omega_L$ is also observed in the upper panel of Fig. 6. This spectral component is spurious with little influence on the population dynamics. The broad spectrum of Fig. 6(a) is in contrast to that obtained by optimization under the spectral constraint which yields a perfect nonresonant two-photon solution [cf. Fig. 6(c)], demonstrating the effectiveness of the spectral constraint. In both cases, the $|3s\rangle$ state is completely depleted and later refilled; cf. the black lines in Figs. 6(b) and 6(d).

The effect of a state-dependent constraint is studied in Fig. 7 for increasing weight of the constraint, $\lambda_b T$. The allowed subspace is now defined as $\{|3s\rangle, |4s\rangle, |7p\rangle\}$. As indicated by the very different population dynamics observed in Figs. 7(d)–7(f), the optimization identifies very different
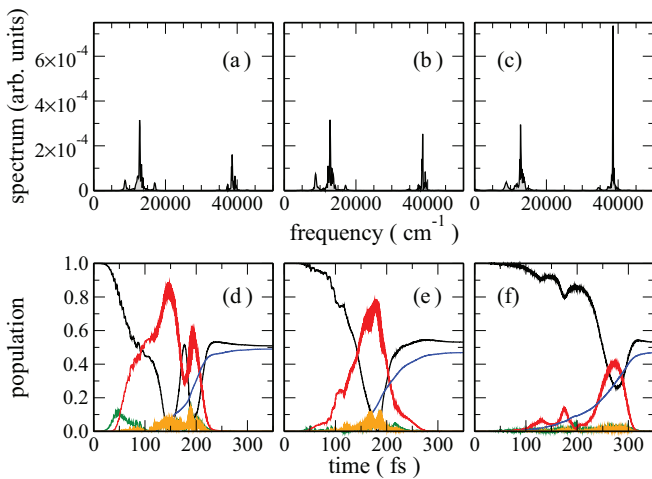

FIG. 7. (Color online) Control of harmonic generation with a state-dependent constraint: (a)–(c) Spectra and (d)–(f) population dynamics for optimization with (a),(d) $\lambda_b T = -0.5$, (b),(e) $\lambda_b T = -1.0$, and (c),(f) $\lambda_b T = -1.5$, and a 50 fs guess pulse with $E_2 = 0.000\,201$ a.u., $\lambda_0 = 400$.
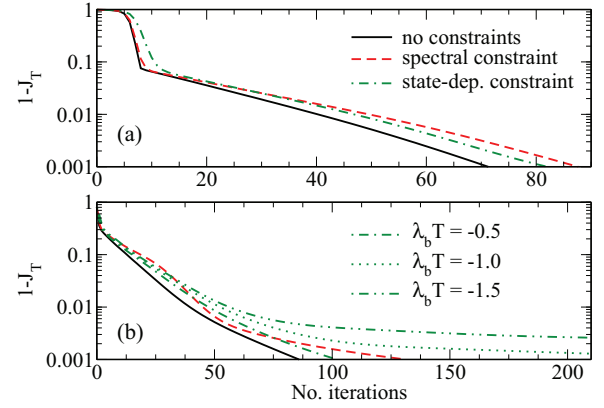

FIG. 8. (Color online) Convergence toward the optimum with spectral constraint, state-dependent constraint, and no constraint for (a) two-photon absorption and (b) harmonic generation. The parameters in (a) correspond to those of Fig. 5; the parameters in (b) correspond to those of Fig. 7.

solutions when changing the weight of the constraint. However, the corresponding spectra are very complex, i.e., none of these solutions resemble the simple spectrum obtained by optimization with the spectral constraint; cf. Fig. 6(c). Increasing the weight $\lambda_b T$ leads to larger widths of each of the spectral peaks, with the optimized spectrum for the largest value of $\lambda_b T$ containing also a peak at $5\omega_L$ [not shown on the scale of Fig. 7(f)]. Although the two-photon peak is central for the population dynamics (cf. the red lines in the lower part of Fig. 7), the contribution of the additional peaks is needed to realize the desired population transfer.

The convergence behavior of the optimization algorithm for maximizing two-photon absorption (upper panel) and maximizing the transition dipole of the $|3s\rangle \rightarrow |7p\rangle$ transition (lower panel) is shown in Fig. 8, comparing spectral (red dashed line), state-dependent (green dotted and dash-dotted lines), and no (black solid line) constraint. Not surprisingly, restricting the search by additional constraints increases the number of iterations to reach a prespecified value of the target functional. Which of the constraints, spectral or state dependent, requires more iterations depends on the weights λ_a^i and $\lambda_b T$. The dotted and double-dot-dashed green curves in Fig. 8(b) reach $1 - J_T = 10^{-3}$ after 347, respectively 3146, iterations. This illustrates that too large a value of the weight can lead the algorithm to become stuck. For both constraints, the additional numerical effort is not only due to a larger number of iterations. While the Fredholm equation (12) needs to be solved for the spectral constraint as discussed above, the state-dependent constraint requires backward propagation with an inhomogeneous Schrödinger equation; cf. Eq. (17). Since the latter requires more applications of the Hamiltonian than propagation for a regular Schrödinger equation [35], the numerical effort due to the inhomogeneity increases with system complexity. This is in contrast to the spectral constraint where the additional effort due to the constraint is independent of the system complexity and depends only on the number of points used in the time discretization. This represents another important advantage of the spectral constraint approach.

IV. CONTROL OF VIBRATIONAL POPULATION TRANSFER

We apply Krotov's method using a spectral constraint to a second example, i.e., vibrational population transfer in Rb_2 molecules. Our model accounts for the 32 lowest vibrational levels in each of two electronic states: the $X^1\Sigma_g^+$ ground state and the $(1)^1\Sigma_u^+$ electronically excited state. The details of the model are found in Ref. [12]. The time-dependent Schrödinger equation for the forward and backward propagation, given by Eq. (1), is solved using a Chebychev propagator [37] and 16 384 time grid points. The guess pulse is chosen to be Gaussian centered around the frequency of the $X^1\Sigma_g^+(v = 0) \rightarrow (1)^1\Sigma_u^+(v' = 10)$ transition, and the shape function is the same as in Sec. III.

The optimization goal consists of driving population from $v = 10$ to $v = 0$, both in the electronic ground state, using Raman transitions via the electronically excited state. This type of population transfer is known to yield optimized pulses with very broad spectra [14,31]. We therefore apply a spectral constraint to see whether solutions with more favorable spectra exist and can be identified. Obviously, a state-dependent constraint is of no use in this context, since the many spectral components are not easily connected to specific levels that could then be assigned to the forbidden subspace.

The results of optimization with and without spectral constraint are shown in Fig. 9 for a Gaussian guess pulse with central frequency $\omega_L = 11\,127$ cm^{-1}, corresponding to the transition frequency $\omega_{v=0,v'=10}$, peak amplitude $E_0 = 10^{-4}$ a.u. and pulse duration of 960 fs. In addition to the peak of the guess pulse and an obvious peak at $\omega_{v=10,v'=10} = 10\,565$ cm^{-1}, the spectrum obtained by optimization without constraint contains peaks at 9440 cm^{-1}, 10 000 cm^{-1}, and 11 676 cm^{-1}; cf. Fig. 9(a). These peaks are not spurious: When removed from the pulse, the population in the target level $v = 0$

is reduced by more than 10%; cf. the red dashed and green dot-dashed lines in Fig. 9(b). When using the new algorithm with filters at those frequencies, the spectral amplitudes are largely reduced. Their influence on the population dynamics is negligible, as seen by the red dashed and green dot-dashed lines in Fig. 9(d), which are nearly indistinguishable.

This example demonstrates the effectiveness of the spectral constraint for a system which is too complex to guess a simple solution to the control problem. Indeed, optimization with and without spectral constraint yields distinct solutions with different spectral properties.

V. CONCLUSIONS

We have shown how additional constraints can be used in quantum optimal control to steer the optimization pathway towards one desired solution out of several possible ones. We have considered nonresonant excitation of atoms and vibrational Raman transfer in molecules. In order to enforce nonresonant absorption, both a spectral constraint and a state-dependent constraint are effective in suppressing resonant excitation pathways. However, only the spectral constraint yields simple spectra without spurious peaks. For vibrational population transfer using Raman transitions, the spectral constraint allows for finding solutions with minimal spectral support. This is in contrast to unconstrained optimization which yields spectra consisting of several peaks that are all relevant for reaching the final-time target. There also exist control problems where the state-dependent constraint represents the best-suited approach, for example when avoiding population transfer to states that are resonant with the main pulse frequencies [12]. In this case, the spectral constraint would not be helpful. In all of these examples, the additional constraint allows for identifying different control strategies than those obtained by unconstrained optimization. A similar conclusion is reached by a related investigation of the control of molecular orientation using state-dependent and time constraints [42].

Both constraints imply a larger numerical cost than the standard optimization without additional constraints. They lead to a moderate increase in the number of iterations required to reach a prespecified value of the final-time target. This reflects that a constrained control problem is harder to solve. Moreover, the spectral constraint requires solution of an implicit integral equation for the change in the control, whereas an inhomogeneous Schrödinger equation needs to be solved when using the state-dependent constraint. Notably, the additional numerical effort for the spectral constraint is independent of system size and depends only on the number of points used in the time discretization.

In summary, most quantum control problems provide many solutions. In order to select the "best" solution, it is crucial to employ a mathematical formulation of additional constraints that closely captures the physical desiderata. Spectral constraints represent a particularly important class of constraints since the pulse bandwidth in any experiment is necessarily finite. Moreover, smooth spectra with minimal support are typically associated with more robust solutions. A possible connection between spectral constraints and robustness of the control will be the subject of future work.
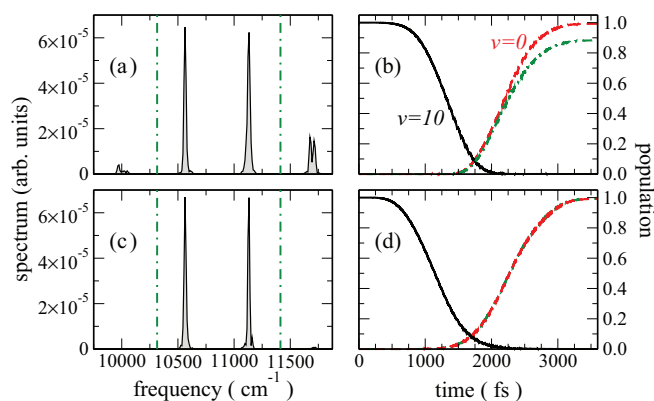

FIG. 9. (Color online) (a),(c) Spectra and (b),(d) population dynamics for vibrational Raman transfer in Rb_2 molecules from $v = 10$ to $v = 0$ optimized (c),(d) with and (a),(b) without spectral constraint using $\lambda_0 = 1000$. The bandwidth constraint consists of filters at 9440 cm^{-1}, 10 000 cm^{-1}, and 11 676 cm^{-1} with $\sigma_i = 220$ cm^{-1} and $\lambda_a^i = 10^5$ $\forall i$. The green dot-dashed lines in (b),(d) represent the population in $v = 0$ for pulses where all spectral amplitude outside the interval indicated by the vertical green lines in (a),(c) was removed.

[1] S. A. Rice and M. Zhao, *Optical Control of Molecular Dynamics* (Wiley, New York, 2000).

[2] C. Brif, R. Chakrabarti, and H. Rabitz, New J. Phys. **12**, 075008 (2010).

[3] J. Somlói, V. A. Kazakov, and D. J. Tannor, Chem. Phys. **172**, 85 (1993).

[4] R. S. Judson and H. Rabitz, Phys. Rev. Lett. **68**, 1500 (1992).

[5] H. A. Rabitz, M. M. Hsieh, and C. M. Rosenthal, Science **303**, 1998 (2004).

[6] R. Chakrabarti and H. Rabitz, Int. Rev. Phys. Chem. **26**, 671 (2007).

[7] A. N. Pechen and D. J. Tannor, Phys. Rev. Lett. **106**, 120402 (2011).

[8] M. Wollenhaupt, A. Präkelt, C. Sarpe-Tudoran, D. Liese, and T. Baumert, J. Mod. Opt. **52**, 2187 (2005).

[9] G. Vogt, P. Nuernberger, R. Selle, F. Dimler, T. Brixner, and G. Gerber, Phys. Rev. A **74**, 033413 (2006).

[10] T. Bayer, M. Wollenhaupt, and T. Baumert, J. Phys. B **41**, 074007 (2008).

[11] K. W. Moore and H. Rabitz, J. Chem. Phys. **137**, 134113 (2012).

[12] J. P. Palao, R. Kosloff, and C. P. Koch, Phys. Rev. A **77**, 063412 (2008).

[13] D. M. Reich, J. P. Palao, and C. P. Koch, J. Mod. Opt., doi: 10.1080/09500340.2013.844866.

[14] C. P. Koch, J. P. Palao, R. Kosloff, and F. Masnou-Seeuws, Phys. Rev. A **70**, 013402 (2004).

[15] C. Gollub, M. Kowalewski, and R. de Vivie-Riedle, Phys. Rev. Lett. **101**, 073002 (2008).

[16] M. Lapert, R. Tehini, G. Turinici, and D. Sugny, Phys. Rev. A **79**, 063411 (2009).

[17] M. Schröder and A. Brown, New J. Phys. **11**, 105031 (2009).

[18] D. Meshulach and Y. Silberberg, Nature (London) **396**, 239 (1998).

[19] D. Meshulach and Y. Silberberg, Phys. Rev. A **60**, 1287 (1999).

[20] A. Präkelt, M. Wollenhaupt, C. Sarpe-Tudoran, and T. Baumert, Phys. Rev. A **70**, 063407 (2004).

[21] C. Trallero-Herrero, D. Cardoza, T. C. Weinacht, and J. L. Cohen, Phys. Rev. A **71**, 013423 (2005).

[22] C. Trallero-Herrero, J. L. Cohen, and T. Weinacht, Phys. Rev. Lett. **96**, 063603 (2006).

[23] C. Trallero-Herrero and T. C. Weinacht, Phys. Rev. A **75**, 063401 (2007).

[24] L. Chuntonov, L. Rybak, A. Gandman, and Z. Amitay, Phys. Rev. A **77**, 021403 (2008).

[25] L. Chuntonov, L. Rybak, A. Gandman, and Z. Amitay, J. Phys. B **41**, 035504 (2008).

[26] Z. Amitay, A. Gandman, L. Chuntonov, and L. Rybak, Phys. Rev. Lett. **100**, 193002 (2008).

[27] L. Chuntonov, L. Rybak, A. Gandman, and Z. Amitay, Phys. Rev. A **81**, 045401 (2010).

[28] D. M. Reich, M. Ndong, and C. P. Koch, J. Chem. Phys. **136**, 104103 (2012).

[29] S. E. Sklarz and D. J. Tannor, Phys. Rev. A **66**, 053619 (2002).

[30] A. Konnov and V. Krotov, Autom. Remote Control **60**, 1427 (1999).

[31] M. Ndong and C. P. Koch, Phys. Rev. A **82**, 043437 (2010).

[32] J. P. Palao and R. Kosloff, Phys. Rev. A **68**, 062308 (2003).

[33] W. Volk, Hahn-Meitner-Institut für Kernforschung Berlin, Tech. Report No. HMI-B286, 1979 (unpublished).

[34] W. Volk, J. Integral Eqs. **9**, 171 (1985).

[35] M. Ndong, H. Tal-Ezer, R. Kosloff, and C. P. Koch, J. Chem. Phys. **130**, 124108 (2009).

[36] A. Kramida, Y. Ralchenko, J. Reader, and N. A. Team, *NIST Atomic Spectra Database* (Version 5.0), http://physics.nist.gov/asd.

[37] H. Tal-Ezer and R. Kosloff, J. Chem. Phys. **81**, 3967 (1984).

[38] A. Gandman, L. Chuntonov, L. Rybak, and Z. Amitay, Phys. Rev. A **75**, 031401 (2007).

[39] S. D. Clow, C. Trallero-Herrero, T. Bergeman, and T. Weinacht, Phys. Rev. Lett. **100**, 233603 (2008).

[40] L. Rybak, L. Chuntonov, A. Gandman, N. Shakour, and Z. Amitay, Opt. Express **16**, 21738 (2008).

[41] B. W. Shore, *Manipulating Quantum Structures Using Laser Pulses* (Cambridge University Press, Cambridge, UK, 2011).

[42] M. Ndong, C. P. Koch, and D. Sugny, [J. Mod. Opt. (to be published)], arXiv:1308.0666.